JACS
JOURNAL OF THE AMERICAN CHEMICAL SOCIETY
Article
pubs.acs.org/JACS

Realizing High Figure of Merit in Phase-Separated Polycrystalline $Sn_{1-x}Pb_xSe$

Guodong Tang,*[,†] Wei Wei,[†] Jian Zhang,*[,‡] Yusheng Li,[†] Xiang Wang,[†] Guizhou Xu,[†] Cheng Chang,[∥] Zhihe Wang,[§] Youwei Du,[§] and Li-Dong Zhao*[,∥]

[†]School of Materials Science and Engineering, Nanjing University of Science and Technology, Nanjing 210094, China
[‡]Key Laboratory of Materials Physics, Institute of Solid State Physics, Chinese Academy of Sciences, Hefei 230031, China
[§]National Laboratory of Solid State Microstructures, Department of Physics, Nanjing University, Nanjing 210093, China
[∥]School of Materials Science and Engineering, Beihang University, Beijing 10091, China

Supporting Information

ABSTRACT: Solid-state thermoelectric technology, interconverting heat to electrical energy, offers a promising solution for relaxing global energy problems. A high dimensionless figure of merit *ZT* is desirable for high-efficiency thermoelectric power generation. To date, thermoelectric materials research has focused on increasing the material's *ZT*. Here we first fabricated phase-separated $Sn_{1-x}Pb_xSe$ materials by hydrothermal synthesis. We demonstrate that the simultaneous optimization of the power factor and significant reduction in thermal conductivity can be achieved in the phase-separated $Sn_{1-x}Pb_xSe$ material. The introduction of the PbSe phase contributes to improvement of the electrical conductivity and power factor of the SnSe phase. Meanwhile, nanoscale precipitates and mesoscale grains define all-scale hierarchical architectures to scattering phonons, leading to low lattice thermal conductivity. These two favorable factors lead to remarkably high thermoelectric performance with $ZT \sim 1.7$ at 873 K in polycrystalline SnSe + 1% PbSe along the pressing direction, which is a record-high *ZT* for SnSe polycrystals. These findings highlight the prospects of realizing highly effective solid-state thermoelectric devices.

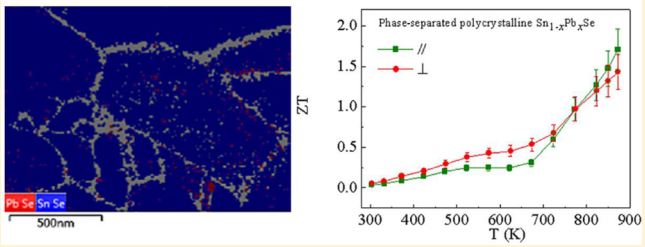

INTRODUCTION

Thermoelectric materials, harvesting electric power directly from heat, are expected to have a significant impact on power generation. The performance of a thermoelectric material is determined by the dimensionless figure of merit *ZT*, defined as $ZT = S^2\sigma T/\kappa$, where *S* is the Seebeck coefficient, σ is the electrical conductivity, *T* is the absolute temperature, and κ is the thermal conductivity. However, the widespread use of thermoelectric technology is constrained by the relatively low conversion efficiency of thermoelectric materials. Persistent efforts have been devoted to improving *ZT* through either boosting the power factor ($S^2\sigma$) or lowering the thermal conductivity. The power factor can be improved via band structure engineering[1,2] or the electron energy filtering effect.[3] Nanostructuring, in particular, has proved to be an effective approach for reducing the thermal conductivity through embedding of nanoscale precipitates in the matrix.[4−6] For example, a nominal PbTe matrix system was shown to reach a *ZT* of ∼2.2 by invoking all-scale hierarchical architectures.[7]

SnSe, which is composed of earth-abundant and environmentally friendly elements, will produce many new, low-cost thermoelectric energy generation opportunities.[8,9] A record *ZT* of ∼2.6 was recently reported in SnSe single crystals along the *b* axis.[8] The remarkable *ZT* was attributed to low thermal conductivity due to giant phonon anharmonicity.[10−12] However, the thermoelectric properties of SnSe single crystals are highly anisotropic.[8] Moreover, the use of single crystals in thermoelectric devices is limited by the need for careful control of the employed conditions required for crystal growth, which is difficult for large-scale industries. In contrast to single crystals, polycrystalline bulk materials can be easily scaled up in industrial applications. However, the peak *ZT* value of polycrystalline SnSe was significantly decreased to less than 1 because of its lower electrical conductivity and higher thermal conductivity.[13] A *ZT* of ∼0.6 at about 750 K was achieved in Ag-doped polycrystalline SnSe by increasing the carrier concentration.[14] To date, a best peak *ZT* of ∼1 was achieved in iodine-doped n-type polycrystalline $SnSe_{1-x}S_x$.[15] To facilitate widespread applications, polycrystalline bulk materials that can generate high *ZT* values must be developed. In thermoelectric materials, alloying (substitution or doping) can not only tune the carrier concentration to optimize the power factor but also induce point defects and adjust the microstructure to reduce the lattice thermal conductivity.[16] Zhao et al.[17] reported that ultrahigh thermoelectric performance can be realized in SnSe

Received: July 12, 2016
Published: September 22, 2016

DOI: 10.1021/jacs.6b07010
J. Am. Chem. Soc. 2016, 138, 13647−13654

single crystals by Na doping through pushing the Fermi level deep into the electronic bands and increasing the carrier concentration. The electronegativities of Pb, Sn, and Se are 2.33, 1.96, and 2.55, respectively, according to the Pauling electronegativity scale. Pb doping can be expected to give rise to a higher carrier concentration as a result of the smaller electronegativity difference between Pb and Se. In addition, the thermoelectric materials fabricated through nanostructured engineering were found to exhibit properties that show promise for thermoelectric applications.[7,18] Phase-separated nanostructured materials were reported to exhibit low thermal conductivity and high thermoelectric performance.[19−21] The lattice thermal conductivity can be significantly suppressed by precipitated nanoscale second phases and phase boundaries as phonon-scattering sources.[19] For instance, a high thermoelectric performance ($ZT_{max} \sim 2.2$) can be achieved in phase-separated 2.5% K-doped $PbTe_{0.7}S_{0.3}$.[19] It is therefore of interest to synergistically optimize the electrical and thermal transport properties of polycrystalline SnSe by tuning the carrier concentration and controlling the structure.

Here we first fabricated phase-separated polycrystalline $Sn_{1-x}Pb_xSe$ by hydrothermal synthesis. We indeed demonstrate that when fractions of PbSe are introduced into the SnSe matrix, significantly enhanced thermoelectric performance can be achieved. We found a giant increase in ZT from 0.5 (SnSe polycrystals) to 1.7 (phase-separated $Sn_{1-x}Pb_xSe$) along the pressing direction at 873 K. Such a high ZT was achieved by synergistically optimizing the electrical and thermal transport properties via carrier concentration tuning and hierarchical architecturing. The phase-separated polycrystalline $Sn_{1-x}Pb_xSe$ outperforms most current commercial thermoelectric materials. The high-performance bulk material facilitates device fabrication and industrial process scale-up. This work may facilitate practical applications in highly effective solid-state thermoelectric systems.

EXPERIMENTAL SECTION

The starting materials were $SnCl_2{\cdot}2H_2O$ (99%, Kelong, China), $PbCl_2$ (99.999%, Sigma-Aldrich, St. Louis, MO, USA), and Se powder (99.9%, Kelong, China). A series of SnSe + x mol % PbSe samples were synthesized using hydrothermal methods. $SnCl_2{\cdot}2H_2O$ and $PbCl_2$ were first dissolved in deionized water. The solution was then sonicated at room temperature for 10 min, followed by addition of NaOH and sonication for another 10 min. The mixture was then transferred to a Teflon-lined stainless steel autoclave of 100 mL capacity, and Se was added, after which the mixture was heated at 403 K for 36 h. After cooling to room temperature, the products were collected and thoroughly washed with absolute ethanol and deionized water several times. The powders were dried at 333 K for 4 h with a vacuum dryer. The above steps were repeated to obtain more dried powders. The dried powders were loaded into a graphite die with a diameter of 10 mm and then densified by spark plasma sintering (HPD 10, FCT System GmbH) at 693 K for 7 min under a uniaxial pressure of 50 MPa. The heating and cooling rates for sintering were 150 and 70 K/min, respectively.

The powder X-ray diffraction (XRD) patterns were obtained on a Bruker D8 Advance instrument with Cu Kα radiation and scanning with a step size of 0.02°. Transmission electron microscopy (TEM) investigations were conducted with a JEOL 2100F microscope. Transmission electron backscatter diffraction (T-EBSD) measurements were performed on a Zeiss Auriga field-emission scanning electron microscope equipped with a Nordlys-Nano EBSD detector. An accelerating voltage of 30 keV was used with a probe current of 1.6 nA and a step size of 4 nm. Samples were prepared for TEM and T-EBSD analysis by focused ion beam (FIB) milling using the in situ lift-out technique on an FEI Nova Nanolab DualBeam instrument.

The Seebeck coefficient and electrical conductivity were measured simultaneously in a helium atmosphere at 300−873 K on an Ulvac-Riko ZEM-3 instrument system. The electrical properties obtained from two independently prepared samples were similar. The thermal diffusivity coefficient (D) was measured at 300−873 K by the laser flash diffusivity method in a Netzsch LFA-457 instrument. The heat capacity (C_p) was measured using differential scanning calorimetry (DSC). The density (ρ) was determined using the dimensions and mass of the sample and then reconfirmed using the Archimedes method. The thermal conductivity was calculated from the expression $\kappa = DC_p\rho$. The thermal conductivities obtained from two independently prepared samples were similar. The Hall coefficient (R_H) was determined using a physical properties measurement system (PPMS-9T). The carrier concentration (n) was calculated as $n = 1/eR_H$, where e is the proton charge. The uncertainty is 5% for the electrical conductivity, 3% for the Seebeck coefficient, and 5% for the thermal conductivity. The combined uncertainty for all of the measurements involved in the calculation of ZT is around 15%.

RESULTS AND DISCUSSION

XRD patterns of SnSe + x mol % PbSe samples are shown in Figure 1a. The SnSe phase with a *Pnma* orthorhombic structure

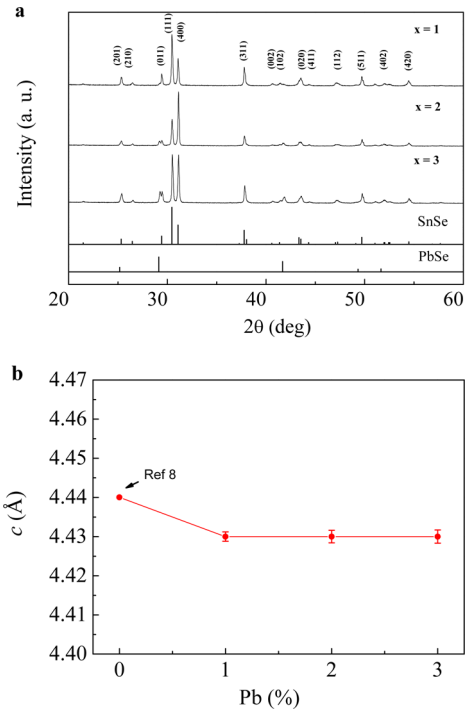

Figure 1. (a) XRD patterns and (b) lattice parameter c of polycrystalline SnSe + x mol % PbSe samples. Standard peaks of PbSe and SnSe are given in (a) for comparison.

can be clearly indexed by matching the strong peaks with the available database. The additional peak that appears near the $(011)_{SnSe}$ peak indicates traces of PbSe in these samples. We examined the microstructures using transmission electron backscatter diffraction (T-EBSD) on the SnSe + 1% PbSe sample. The T-EBSD results provide strong and direct experimental evidence for the existence of the PbSe phase (shown in red in Figure 2a) and the *Pnma* orthorhombic SnSe phase (shown in blue in Figure 2a). The TEM image of the matrix where T-EBSD was performed (Figure 2b) shows that the gray-colored netlike structure in Figure 2a is due to the grain boundaries. The T-EBSD measurements revealed that the dark dots in the TEM image are the PbSe secondary phase, as

DOI: 10.1021/jacs.6b07010
J. Am. Chem. Soc. 2016, 138, 13647−13654

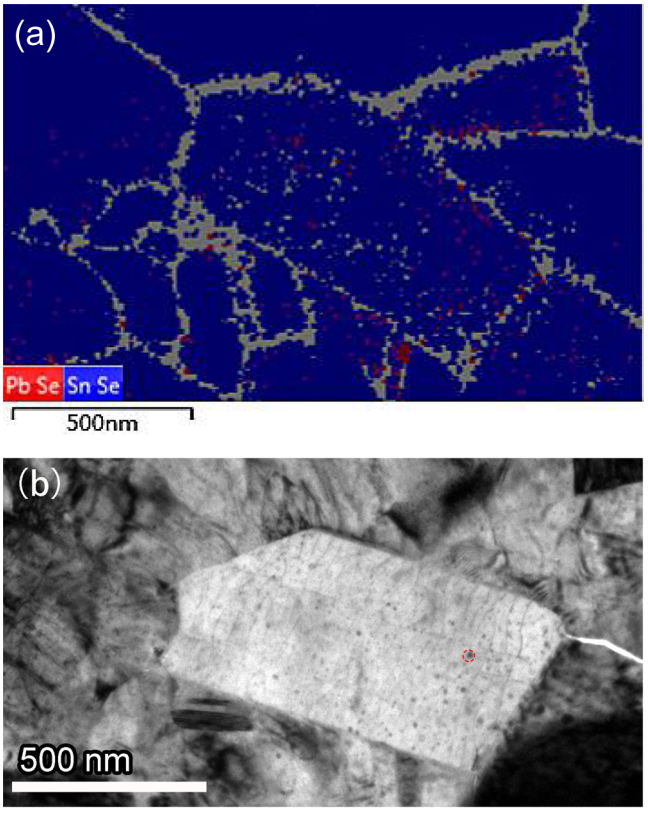

Figure 2. (a) Phase map of SnSe + 1% PbSe with grains identified as the PbSe cubic phase in red and *Pnma* orthorhombic phases in blue from T-EBSD measurements. (b) TEM image of the matrix where T-EBSD was performed.

indicated by the dashed circle in Figure 2b. As shown in Figure 1b and Table S1, the lattice parameters extracted from XRD cell refinement show negligible changes beyond 1% PbSe content, which indicates that the solubility limit must be lower than 1% PbSe. T-EBSD analysis revealed that the amount of the PbSe phase relative to the SnSe phase is around 0.6%. Therefore, we deduce that the solution limit is somewhere around 0.4% PbSe on the basis of the T-EBSD results. T-EBSD orientation maps provide evidence of the randomly oriented texture of the sample (Figure 3).

Figure 4a shows the electrical conductivity (σ) as a function of temperature for SnSe + x mol % PbSe samples measured perpendicular to the pressing direction. The data were compared with those of SnSe single crystals,[8] a typical bulk polycrystalline SnSe[13] and polycrystalline SnSe doped with Ag.[14] The values of σ for polycrystalline SnSe with different levels of PbSe show the same temperature-dependence trend. The change trend of σ for the SnSe + x mol % PbSe samples can be described as follows: first, semiconducting transport behavior occurs from 300 to 425 K; then the behavior changes to metallic-like up to 675 K; above that, σ increases until 825 K; finally, there is a nearly temperature-independent trend up to 873 K. The first upturn in σ from 675 to 825 K can be attributed to the thermal excitation of carriers. The second upturn above 825 K can be attributed to a structural transition from *Pnma* to *Cmcm*.[8,22,23] The structural transition from *Pnma* to *Cmcm* occurs at about 785 K, as shown in Figure S1, which presents the temperature dependence of the specific heat for SnSe + x mol % PbSe samples. Compared with the SnSe single crystals, the SnSe + x mol % PbSe materials possess a higher σ,

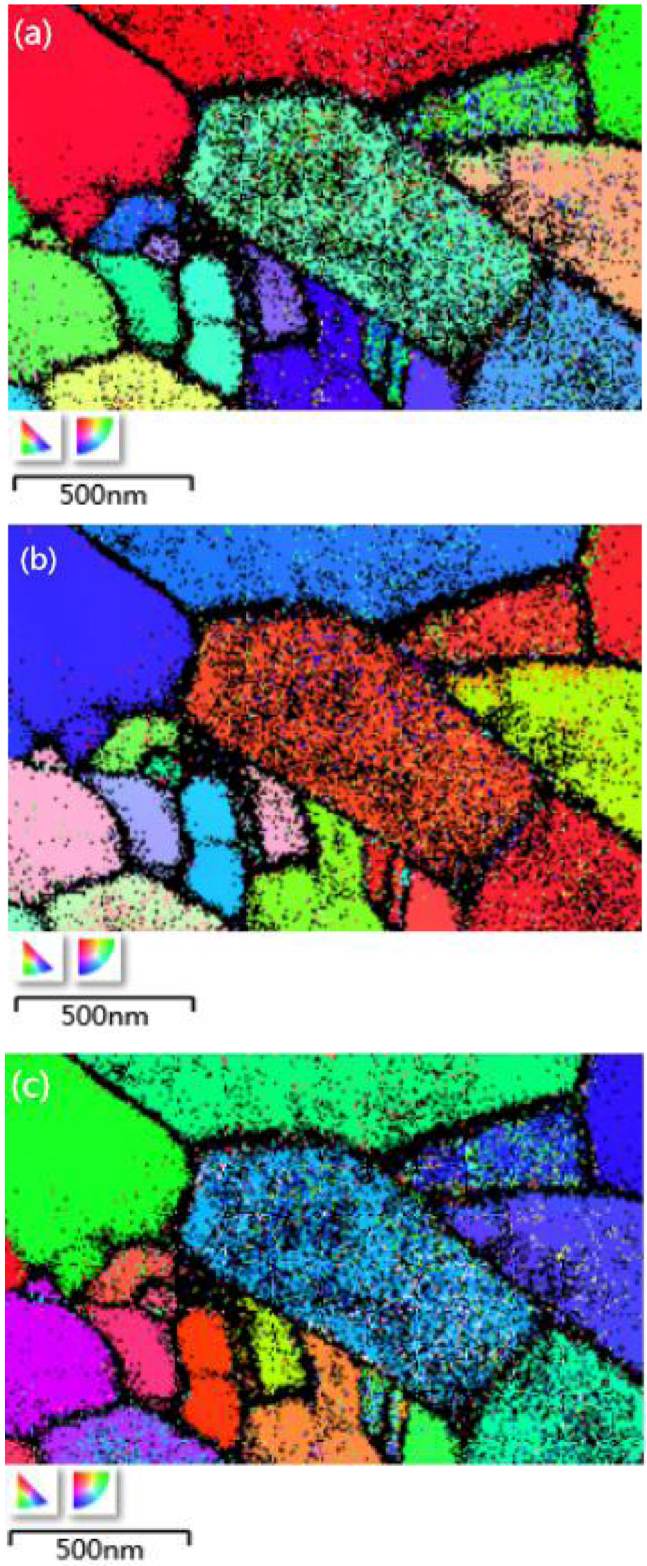

Figure 3. Inverse pole figure (IPF) orientation maps of the SnSe + 1% PbSe sample obtained from T-EBSD: (a) IPF X image; (b) IPF Y image; (c) IPF Z image. The color scheme reflects the orientation with respect to the according axis, as shown in the bottom left-hand corner of each panel.

especially the SnSe + 1% PbSe sample. The σ value for the undoped SnSe single crystals (b axis) exceeds the σ value for the SnSe + 1% PbSe sample only above 823 K. The σ values for

DOI: 10.1021/jacs.6b07010
J. Am. Chem. Soc. 2016, 138, 13647−13654

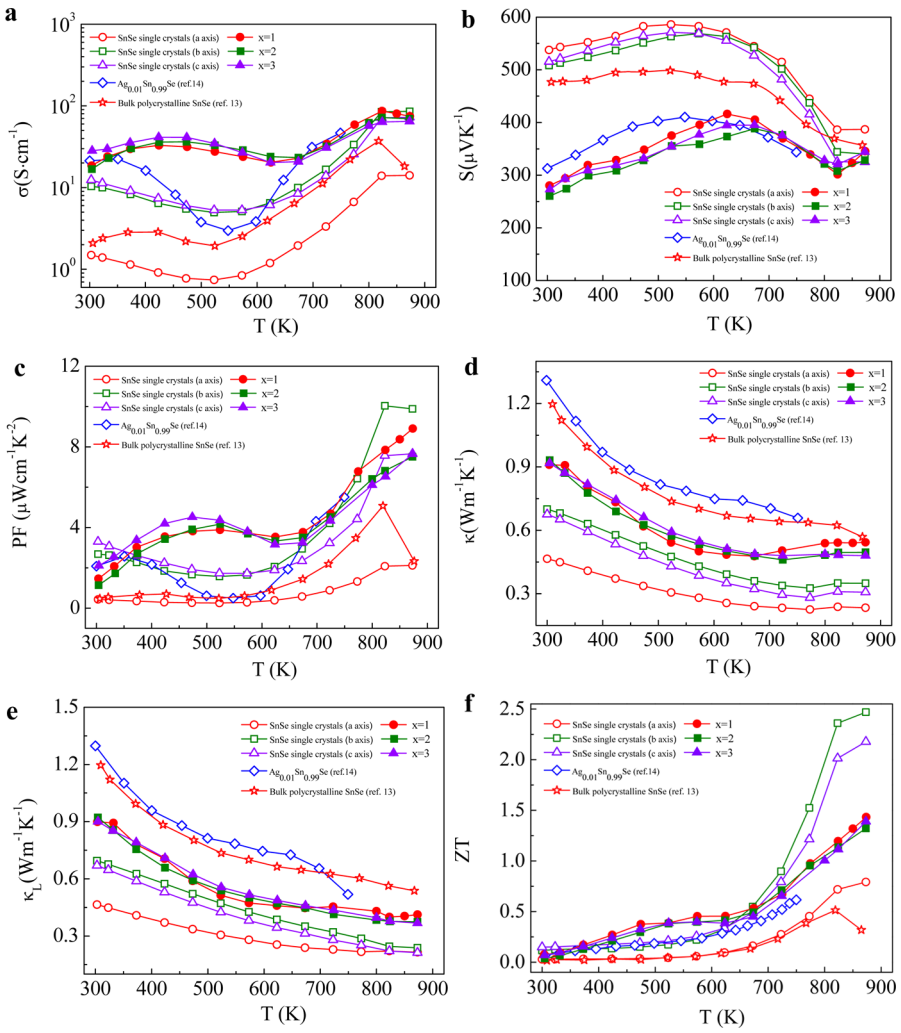

Figure 4. Temperature dependence of (a) electrical conductivity, (b) Seebeck coefficient, (c) power factor, (d) total thermal conductivity, (e) lattice thermal conductivity, and (f) *ZT* for SnSe + *x* mol % PbSe polycrystalline samples measured perpendicular to the pressing direction. Data on the temperature-dependent transport reported for SnSe single crystals,[8] polycrystalline SnSe,[13] and polycrystalline SnSe doped with Ag[14] are shown for comparison.

the SnSe + *x* mol % PbSe samples are significantly larger than that of bulk polycrystalline SnSe. Specifically, the room-temperature σ value is 28.3 S cm^{-1} for SnSe + 3% PbSe, which is larger by 1 order of magnitude than that of typical polycrystalline SnSe (2.1 S cm^{-1}).[13] The electronegativity difference between Pb (2.33) and Se (2.55) is smaller than that between Sn (1.99) and Se (2.55). Pb substitution can be expected to give rise to a higher carrier concentration because of the smaller electronegativity difference. The enhanced carrier concentration was confirmed by Hall measurements. The Hall carrier concentration as a function of PbSe content at 300 K is presented in Figure S2. With increasing PbSe phase content, the carrier concentration increases gradually. The carrier concentrations of SnSe + *x* mol % PbSe samples are larger by 1 order of magnitude than that for PbSe-free SnSe polycrystals.[13] For example, the room-temperature carrier concentration (n) is limited to only ~4 × 10^{17} cm^{-3} for polycrystalline SnSe[13] and increases to 6.1 × 10^{18} cm^{-3} for SnSe + 1% PbSe. Furthermore, the PbSe secondary phase has much better electrical conductivity than the SnSe phase[24] because of the smaller band gap (0.3 eV[25] in contrast to 0.61 eV for the orthorhombic *Pnma* phase[8]). Therefore, the introduction of the PbSe phase contributes to an improvement in the electrical conductivity of the SnSe phase. The enhanced carrier concentration and the introduction of the PbSe phase ultimately contribute to the enhanced σ ($\sigma = ne\mu$) of the SnSe + *x* mol % PbSe materials relative to the σ of single-phase SnSe materials.[19]

Figure 4b shows the temperature dependence of the Seebeck coefficient (S) for all of the SnSe + *x* mol % PbSe samples measured perpendicular to the pressing direction. The SnSe + *x* mol % PbSe materials have lower S values than the undoped single crystals and reported polycrystalline SnSe. We also note that the SnSe + *x* mol % PbSe materials show S values comparable to that of Ag-doped polycrystalline SnSe ($Ag_{0.01}Sn_{0.99}Se$).[14] The SnSe/PbSe phase-separated material has a lower band gap, which should facilitate the excitation of electron−hole pairs, thereby lowering S. The reduction in S is consistent with the enhanced n confirmed by Hall measurements. S increases as the temperature increases, reaching a maximum value in the range of 650−675 K. The Seebeck coefficient peak indicates the onset of bipolar conduction. The slight structure change[26] induces bipolar conduction to occur as the temperature increases. The Seebeck coefficient peaks of the

DOI: 10.1021/jacs.6b07010
J. Am. Chem. Soc. 2016, 138, 13647−13654

obtained polycrystalline samples were pushed to a higher temperature compared with that of the SnSe single crystals.[8] The absolute values of S decrease as the temperature enters the intrinsic range of these materials. Minority carriers (electrons) are produced by transfer of heat-excited holes from the valence band to the conduction band, which adversely affects S at the intrinsic range of temperature. The increase in S for $T > 823$ K is a sign of the phase transition.[22,23,27] The *Cmcm* phase may contribute to the increase in S. The same behavior was also observed in other SnSe polycrystals.[28,29] The power factor (PF), calculated according to the equation of PF = $S^2\sigma$, is presented in Figure 4c. The SnSe + 1% PbSe material has the highest PF among all SnSe + x mol % PbSe samples. The largest PF value, 8.9 μW cm^{-1} K^{-2}, which is obtained at 873 K in this material, is about 4 times higher than that of SnSe polycrystals.[13] The introduction of the PbSe phase substantially contributes to the enhancement of the electrical conductivity and PF of the SnSe matrix.

Figure 4d shows the temperature dependence of the total thermal conductivity (κ) of the SnSe + x mol % PbSe samples. The κ values of SnSe + x mol % PbSe are lower than those of typical bulk polycrystalline SnSe[13] and $Ag_{0.01}Sn_{0.99}Se$.[14] Above 673 K, SnSe + 3% PbSe exhibits the lowest κ among the investigated samples. A room-temperature κ value of = 0.91 W m^{-1} K^{-1} was observed for SnSe + 3% PbSe, which decreased to 0.48 W m^{-1} K^{-1} at 873 K. The relatively low κ, together with the enhancement of both the electrical conductivity and PF, helps achieve high ZT in phase-separated polycrystalline SnSe + x mol % PbSe. We calculated the lattice thermal conductivity (κ_L) using the expression $\kappa_L = \kappa - \kappa_e$, in which the carrier thermal conductivity component (κ_e) was estimated using the Wiedeman–Franz law ($\kappa_e = LT/\rho$, where $L = 2.0 \times 10^{-8}$ V^2/K^2). The negligible difference between the total thermal conductivity κ and the lattice counterpart κ_L reveals that phonon transport dominates κ (Figure 4e). Compared with the reported values for polycrystalline SnSe and polycrystalline SnSe doped with Ag, κ_L of the SnSe-PbSe phase-separated materials is significantly reduced. Microstructure analysis of SnSe + 1% PbSe using TEM was performed to comprehend the reduced κ_L. Nanoscale precipitates were clearly found in the matrix (Figure 5a,b), which appear as dark quasi-circular (oval) and elongated shapes with sizes of 10–20 nm. As shown in Figure 5a, the distribution of nanoscale precipitates is not uniform in the matrix. Selected-area electron diffraction (SAED) was performed on the grains enclosed in areas 1 and 2 in Figure 5a. In the corresponding SAED patterns (Figure 5c,d), which include both the matrix and the secondary phases, Bragg diffraction spots consistent with those of the SnSe matrix and PbSe secondary phases can be observed. The SAED results further confirmed that the $Sn_{1-x}Pb_xSe$ materials separate into SnSe and PbSe phases. Nanoscale precipitates were confirmed to be the PbSe secondary phases by SAED, as indicated by the dashed circle in Figure 5b. Besides nanoscale precipitates, the presence of mesoscale grains around 1 μm (0.35–1.4 μm in size) is evident in Figure 6. Nanoscale precipitates and mesoscale grains form hierarchical structures, which were clearly identified by TEM experiments. The T-EBSD orientation map of the sample, as shown in Figure 3, confirmed that the material has a hierarchical microstructure. Mesoscale grains, which are long-wavelength phonon scattering centers, combined with nanoscale precipitates define all-hierarchical architectures to scatter phonons. This significantly diminishes the lattice thermal conductivity through more effective phonon scattering, resulting in a significant reduction of κ_L compared with the values for PbSe-free SnSe polycrystals and polycrystalline SnSe doped with Ag. Therefore, an overall decrease in κ_L of SnSe + x mol % PbSe compared with the reported bulk polycrystalline SnSe and polycrystalline SnSe doped with Ag was observed. However, the κ_L values of the SnSe/PbSe phase-separated materials are still higher than the reported exceptionally low lattice thermal conductivity of SnSe single crystals.[8]

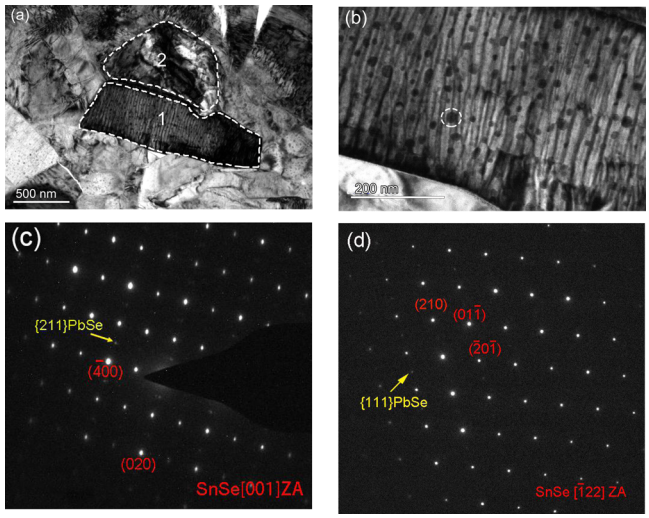

Figure 5. Microstructures of the SnSe + 1% PbSe sample. (a) Low-magnification TEM image. (b) Medium-magnification TEM image showing the presence of nanoscale precipitates. (c, d) SAED patterns measured on one crystallite in (c) area 1 and (d) area 2 shown in (a).

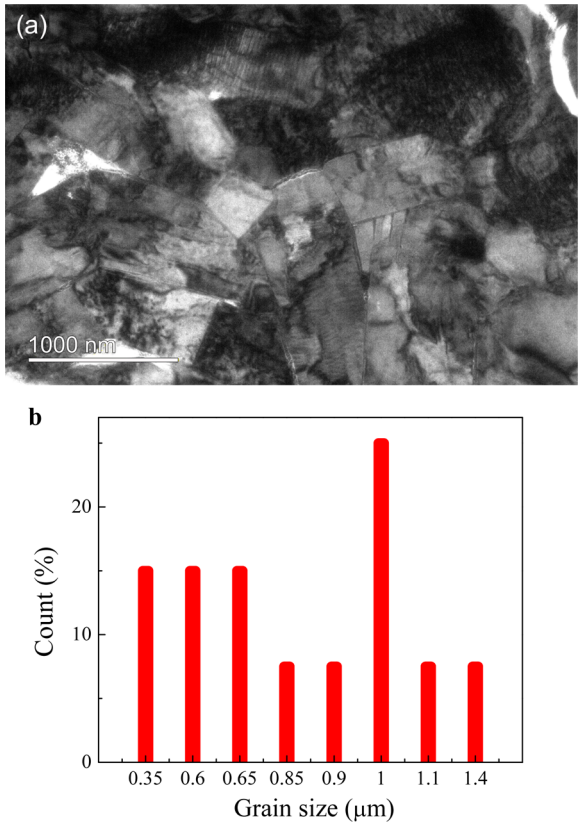

Figure 6. (a) TEM images revealing mesoscale grains. (b) Grain size distribution histogram for the sample in (a).

DOI: 10.1021/jacs.6b07010
J. Am. Chem. Soc. 2016, 138, 13647–13654

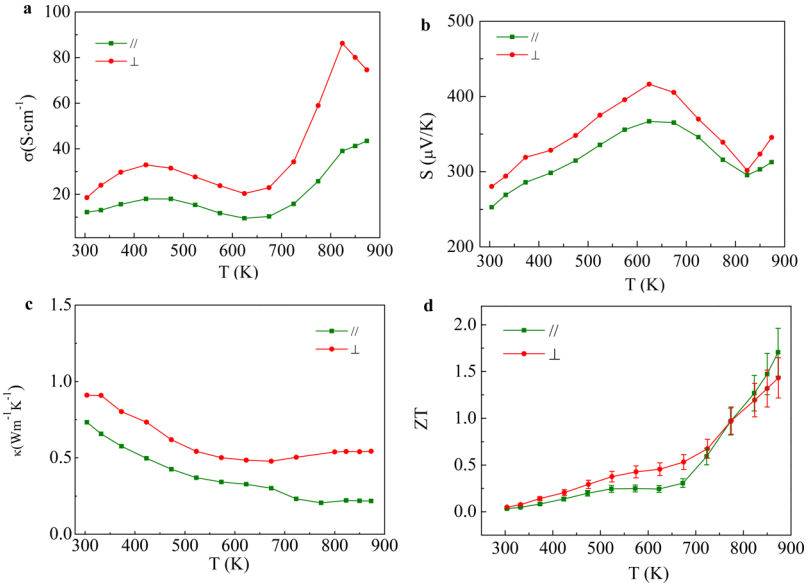

Figure 7. Temperature dependence of (a) electrical conductivity, (b) Seebeck coefficient, (c) thermal conductivity, and (d) *ZT* for SnSe + 1% PbSe along the pressing direction (//) and perpendicular to the pressing direction (⊥). An ultrahigh *ZT* value of ∼1.7 was obtained at 873 K along the pressing direction.

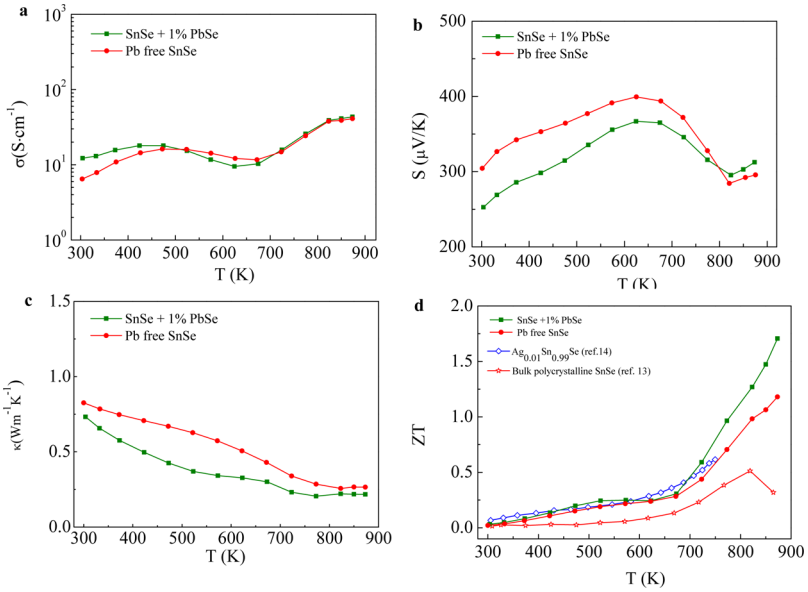

Figure 8. Temperature dependence of (a) electrical conductivity, (b) Seebeck coefficient, (c) thermal conductivity, and (d) *ZT* for SnSe + 1% PbSe and Pb-free SnSe prepared by the same process.

ZT for the SnSe + *x* mol % PbSe samples perpendicular to the pressing direction and those of SnSe single crystals, typical polycrystalline SnSe, and polycrystalline SnSe doped with Ag are compared in Figure 4f as a function of temperature. The SnSe + *x* mol % PbSe materials possess higher *ZT* than the SnSe single crystals below 673 K. The undoped SnSe single crystals (*b* axis and *c* axis) exceed the *ZT* of SnSe + *x* mol % PbSe only at temperatures above 673 K thanks to their ultralow thermal conductivity. The *ZT* values for SnSe + *x* mol % PbSe are significantly larger than those reported for polycrystalline SnSe and polycrystalline SnSe doped with Ag. As shown in Figure 4f, *ZT* for SnSe + 1% PbSe reaches a maximum of ∼1.4 at 873 K. Bulk polycrystalline SnSe shows anisotropy in its transport properties due to the anisotropic crystal structure of this compound.[14,15] The above results show that the SnSe + 1% PbSe material exhibits excellent performance among several samples. Therefore, we further studied its transport properties along the pressing direction. The Seebeck coefficient and electrical conductivity along the pressing direction are lower than those perpendicular to the pressing direction (Figure 7a,b). The difference between the two measured directions for electrical conductivity mainly comes from the outstanding anisotropy of the effective mass.[30] On the basis of the Fermi surface calculation results, the effective mass possesses the highest value along the *a*-axis direction (corresponding to the direction perpendicular to the SnSe layers), meaning a higher effective mass along the pressing direction.[31] High effective band mass results in low mobility.[30,32] Therefore, σ is higher perpendicular to the pressing direction than along the pressing direction because of the larger mobility. The carrier

DOI: 10.1021/jacs.6b07010
J. Am. Chem. Soc. 2016, 138, 13647−13654

concentration is similar along the two directions. As shown in Figure 7a, a more obvious temperature dependence of σ can be observed perpendicular to the pressing direction. The rapid change in σ should favor higher S perpendicular to the pressing direction since $S \sim d(\ln \sigma)/dE$.[31,33] As a result, S perpendicular to the pressing direction is higher than that along the pressing direction. However, ultralow thermal conductivity along the pressing direction was obtained (Figure 7c). A high ZT of 1.7 at 873 K was achieved in bulk polycrystalline SnSe + 1% PbSe along this direction (Figure 7d), in contrast to 0.5 and 0.6 for undoped polycrystalline SnSe[13] and polycrystalline SnSe doped with Ag.[14] Good experimental repeatability of the electrical and thermal transport properties and high ZT were achieved (Figure S4). This is a record ZT value in bulk SnSe polycrystals, which outperform most of the current commercial thermoelectric materials.The thermoelectric properties of Pb-free SnSe prepared by the same process are presented and compared with those of SnSe + 1% PbSe (Figure 8). The XRD results for Pb-free SnSe indicate the coexistence of cubic-phase SnSe and *Pnma* orthorhombic-phase SnSe (Figure S5). We note that κ of the Pb-doped sample is depressed compared with that of Pb-free SnSe (Figure 8c). As a result, ZT of SnSe + 1% PbSe is significantly larger than that of pristine SnSe (Figure 8d). It is worth noting that Pb-free SnSe exhibits excellent thermoelectric performance compared with typical polycrystalline SnSe[13] because of the lower thermal conductivity of Pb-free SnSe.

CONCLUSION

We applied a cost-effective method to produce a high-performance bulk thermoelectric material. The electrical and thermal transport properties of polycrystalline SnSe were synergistically optimized by tuning of the carrier concentration and control of the structure. The introduction of the PbSe phase contributes to a significant enhancement of the electrical conductivity and power factor of the SnSe phase. Meanwhile, all-scale hierarchical architectures significantly diminish the lattice conductivity. The ZT values of phase-separated SnSe + x mol % PbSe materials are significantly larger than those reported for polycrystalline SnSe. The phase-separated SnSe + 1% PbSe material shows high ZT values of 1.7 and 1.4 parallel and perpendicular to the pressing direction, respectively. A giant increase in ZT from 0.5 (SnSe polycrystals) to 1.7 (phase-separated $Sn_{1-x}Pb_xSe$) was achieved. The significant increase in ZT for polycrystalline SnSe may open realistic pathways to practical applications in waste heat recovery and power generation.

ASSOCIATED CONTENT

Supporting Information

The Supporting Information is available free of charge on the ACS Publications website at DOI: 10.1021/jacs.6b07010.

Lattice parameters (Table S1), temperature dependence of the specific heat (Figure S1), Hall carrier concentration (Figure S2), carrier mobility as a function of PbSe content (Figure S3), reproducibility of the thermoelectric properties as a function of temperature for SnSe + 1% PbSe measured along the pressing direction (Figure S4), and XRD pattern of Pb-free SnSe (Figure S5) (PDF)

AUTHOR INFORMATION

Corresponding Authors

*tangguodong@njust.edu.cn

*zhangjian@issp.ac.cn

*zhaolidong@buaa.edu.cn

Notes

The authors declare no competing financial interest.

ACKNOWLEDGMENTS

This work was supported by the National Natural Science Foundation of China (11204134 and 51571007), Natural Science Foundation of Jiangsu Province (BK20161495), the Priority Academic Program Development of Jiangsu Higher Education Institutions, the "Zhuoyue" Program of Beihang University, and the Recruitment Program for Young Professionals.

REFERENCES

(1) Heremans, J. P.; Jovovic, V.; Toberer, E. S.; Saramat, A.; Kurosaki, K.; Charoenphakdee, A.; Yamanaka, S.; Snyder, G. J. *Science* **2008**, *321*, 554.

(2) Pei, Y. Z.; Shi, X. Y.; LaLonde, A.; Wang, H.; Chen, L. D.; Snyder, G. J. *Nature* **2011**, *473*, 66.

(3) Zide, J. M. O.; Vashaee, D.; Bian, Z. X.; Zeng, G.; Bowers, J. E.; Shakouri, A.; Gossard, A. C. *Phys. Rev. B: Condens. Matter Mater. Phys.* **2006**, *74*, 205335.

(4) Hsu, K. F.; Loo, S.; Guo, F.; Chen, W.; Dyck, J. S.; Uher, C.; Hogan, T.; Polychroniadis, E. K.; Kanatzidis, M. G. *Science* **2004**, *303*, 818.

(5) Zhao, X. B.; Ji, X. H.; Zhang, Y. H.; Zhu, T. J.; Tu, J. P.; Zhang, X. B. *Appl. Phys. Lett.* **2005**, *86*, 062111.

(6) Poudel, B.; Hao, Q.; Ma, Y.; Lan, Y. C.; Minnich, A.; Yu, B.; Yan, X.; Wang, D. Z.; Muto, A.; Vashaee, D.; Chen, X. Y.; Liu, J. M.; Dresselhaus, M. S.; Chen, G.; Ren, Z. F. *Science* **2008**, *320*, 634.

(7) Biswas, K.; He, J. Q.; Blum, I. D.; Wu, C. I.; Hogan, T. P.; Seidman, D. N.; Dravid, V. P.; Kanatzidis, M. G. *Nature* **2012**, *489*, 414.

(8) Zhao, L. D.; Lo, S. H.; Zhang, Y. S.; Sun, H.; Tan, G. J.; Uher, C.; Wolverton, C.; Dravid, V. P.; Kanatzidis, M. G. *Nature* **2014**, *508*, 373.

(9) Peng, K. L.; Lu, X.; Zhan, H.; Hui, S.; Tang, X. D.; Wang, G. W.; Dai, J. Y.; Uher, C.; Wang, G. Y.; Zhou, X. Y. *Energy Environ. Sci.* **2016**, *9*, 454.

(10) Li, C. W.; Hong, J.; May, A. F.; Bansal, D.; Chi, S.; Hong, T.; Ehlers, G.; Delaire, O. *Nat. Phys.* **2015**, *11*, 1063.

(11) Heremans, J. P. *Nat. Phys.* **2015**, *11*, 990.

(12) Carrete, J.; Mingo, N.; Curtarolo, S. *Appl. Phys. Lett.* **2014**, *105*, 101907.

(13) Sassi, S.; Candolfi, C.; Vaney, J. B.; Ohorodniichuk, V.; Masschelein, P.; Dauscher, A.; Lenoir, B. *Appl. Phys. Lett.* **2014**, *104*, 212105.

(14) Chen, C. L.; Wang, H.; Chen, Y. Y.; Day, T.; Snyder, G. J. *J. Mater. Chem. A* **2014**, *2*, 11171.

(15) Zhang, Q.; Chere, E. K.; Sun, J. Y.; Cao, F.; Dahal, K.; Chen, S.; Chen, G.; Ren, Z. F. *Adv. Energy Mater.* **2015**, *5*, 1500360.

(16) Fu, C. G.; Bai, S. Q.; Liu, Y. T.; Tang, Y. S.; Chen, L. D.; Zhao, X. B.; Zhu, T. J. *Nat. Commun.* **2015**, *6*, 8144.

(17) Zhao, L. D.; Tan, G. J.; Hao, S. Q.; He, J. Q.; Pei, Y. L.; Chi, H.; Wang, H.; Gong, S. K.; Xu, H. B.; Dravid, V. P.; Uher, C.; Snyder, G. J.; Wolverton, C.; Kanatzidis, M. G. *Science* **2016**, *351*, 141.

(18) Dresselhaus, M. S.; Chen, G.; Tang, M. Y.; Yang, R.; Lee, H.; Wang, D. Z.; Ren, Z. F.; Fleurial, J. P.; Gogna, P. *Adv. Mater.* **2007**, *19*, 1043.

(19) Wu, H. J.; Zhao, L. D.; Zheng, F. S.; Wu, D.; Pei, Y. L.; Tong, X.; Kanatzidis, M. G.; He, J. Q. *Nat. Commun.* **2014**, *5*, 4515.

(20) He, J.; Girard, S. N.; Kanatzidis, M. G.; Dravid, V. P. *Adv. Funct. Mater.* **2010**, *20*, 764.

(21) Zhao, L. D.; He, J. Q.; Wu, C.; Hogan, T. P.; Zhou, X. Y.; Uher, C.; Dravid, V. P.; Kanatzidis, M. G. *J. Am. Chem. Soc.* **2012**, *134*, 7902.

(22) Chattopadhyay, T.; Pannetier, J.; Vonschnering, H. G. *J. Phys. Chem. Solids* **1986**, *47*, 879.

DOI: 10.1021/jacs.6b07010
J. Am. Chem. Soc. 2016, 138, 13647−13654

(23) Peters, M. J.; Mcneil, L. E. *Phys. Rev. B: Condens. Matter Mater. Phys.* **1990**, *41*, 5893.
(24) Zhang, Q. Y.; Wang, H.; Liu, W. S.; Wang, H. Z.; Yu, B.; Zhang, Q.; Tian, Z. T.; Ni, G.; Lee, S.; Esfarjani, K.; Chen, G.; Ren, Z. F. *Energy Environ. Sci.* **2012**, *5*, 5246.
(25) Wang, H.; Gibbs, Z. M.; Takagiwa, Y.; Snyder, G. J. *Energy Environ. Sci.* **2014**, *7*, 804.
(26) Adouby, K.; Perez-Vicente, C.; Jumas, J. C.; Fourcade, R.; Touré, A. A. *Z. Kristallogr. - Cryst. Mater.* **1998**, *213*, 343.
(27) Chere, E. K.; Zhang, Q.; Dahal, K.; Cao, F.; Mao, J.; Ren, Z. F. *J. Mater. Chem. A* **2016**, *4*, 1848.
(28) Guo, H. F.; Xin, H. X.; Qin, X. Y.; Zhang, J.; Li, D.; Li, Y. Y.; Song, C. J.; Li, C. *J. Alloys Compd.* **2016**, *689*, 87.
(29) Fu, Y. J.; Xu, J. T.; Liu, G. Q.; Yang, J. K.; Tan, X. J.; Liu, Z.; Qin, H. M.; Shao, H. Z.; Jiang, H. C.; Liang, B.; Jiang, J. *J. Mater. Chem. C* **2016**, *4*, 1201.
(30) Leng, H. Q.; Zhou, M.; Zhao, J.; Han, Y. M.; Li, L. F. *RSC Adv.* **2016**, *6*, 9112.
(31) Kutorasinski, K.; Wiendlocha, B.; Kaprzyk, S.; Tobola, J. *Phys. Rev. B: Condens. Matter Mater. Phys.* **2015**, *91*, 205201.
(32) Pei, Y.; Wang, H.; Snyder, G. *Adv. Mater.* **2012**, *24*, 6125.
(33) (a) Ziman, J. M. *Electrons and Phonons*; Oxford University Press: New York, 2001. (b) Ziman, J. M. *Principles of the Theory of Solids*, 2nd ed.; Cambridge University Press: Cambridge, U.K., 1995.

DOI: 10.1021/jacs.6b07010
J. Am. Chem. Soc. 2016, 138, 13647−13654